Pore-Scale Behavior of Darcy Flow in Static and Dynamic Porous Media

M. Aminpour,[1,2,*] S. A. Galindo-Torres,[1,2,3] A. Scheuermann,[1,2] and L. Li[2]

[1]*Geotechnical Engineering Center, School of Civil Engineering,*
The University of Queensland, Brisbane QLD 4072, Australia
[2]*Research Group on Complex Processes in Geo-Systems, School of Civil Engineering,*
The University of Queensland, Brisbane QLD 4072, Australia
[3]*Department of Civil Engineering and Industrial Design, The University of Liverpool,*
Liverpool L69 3BX, United Kingdom

Lattice-Boltzmann numerical simulations are conducted to explore the pore-scale flow behavior inside modeled porous media over the Darcy regime. We use static (fixed) and dynamic (rotating) particles to form the porous media. The pore flow behavior (tortuosity) is found to be constant in the static medium within the Darcy range. However, the study reveals distinctively different flow structures in the dynamic case depending on the macroscopic Darcy flow rate and the level of internal energy imposed to the system (via the angular velocity of particles). With small Darcy flow rates, tortuous flow develops with vortices occupying a large portion of the pore space but contributing little to the net flow. The formation of the vortices is linked to spatial fluctuations of local pore fluid pressure. As the Darcy flow rate (and, hence, the global fluid pressure gradient across the medium) increases, the effect of local pressure fluctuations diminishes, and the flow becomes more channelized. Despite the large variations of the pore-scale flow characteristics in the dynamic porous media, the macroscopic flow satisfies Darcy's law with an invariant permeability. The applicability of Darcy's law is proven for an internally disturbed flow through porous media. The results raise questions concerning the generality of the models describing the Darcy flow as being channelized with constant (structure-dependent) tortuosity and how the internal sources of energy imposed to the porous media flow are considered.

I. INTRODUCTION

Fluid flow in porous media has been studied extensively across a wide range of disciplines, from mechanical, civil, environmental, chemical, and petroleum engineering, to agricultural, food, material, and biomedical science [1,2]. Numerous natural and artificial systems are controlled or affected by flow in various porous media: for example, seepage flow in soil, multiphase flow of oil, gas, and water in oil reservoirs, contaminant transport within groundwater, and solute movement through biological tissues [3–7], as well as ion transport in fuel cells, and fluid flow in building materials, tablets, textiles, foams, papers, and filters [8–10]. The well-known Darcy's law presents a general method for quantifying the flow in porous media under conditions of small Reynolds numbers (Re), which relates linearly the macroscopic flow velocity V to the fluid pressure gradient across the medium ∇P,

$$V = -\frac{\kappa}{\mu}\nabla P, \qquad (1)$$

with κ and μ being the permeability of the porous medium and dynamic viscosity of the fluid, respectively [note that in

Eq. (1), the effect of gravity is not included [11]]. This law, however, provides no insight into the microscale (pore-scale) flow behavior, which may affect significantly solute and heat-transport processes in the porous medium. Several permeability models have been developed to account for the influence of the porous medium's properties. The classical Kozeny-Carman (KC) equation [12–15] is the most widely used one, as given below

$$\kappa = \frac{\phi^3}{c(1-\phi)^2 S^2}, \qquad (2)$$

where c is the KC constant ($c = c'T^2$ with c' being a constant and T the flow tortuosity), ϕ is the medium's porosity, and S is the specific surface area equal to the ratio of the total interstitial surface area to the volume of solids [11]. The KC equation is derived from the consideration of a simple capillary model, which translates the complex structure of porous media to a set of capillary tubes with a certain length (equal to the tortuosity times as the direct length of the medium). This equation implies a constant flow tortuosity for a given porous medium (of constant ϕ and S) undergoing flow in the Darcy regime (with constant κ). Consequently, the current conceptualizations dealing with

*m.aminpour@uq.edu.au

the flow behavior at the pore scale have assumed the invariant flow patterns (hence, the constant tortuosity) when Darcy's law applies. Experimental [16], analytical [17], theoretical [18], and numerical [19] models have been developed to relate the tortuosity of flow to the porosity of the porous media (see the review in Refs. [20,21]) but not to the flow rate. However, experimental investigations using nuclear-magnetic-resonance velocimetry [22–31] and optical imaging techniques [32–38] have demonstrated extensive variations of pore-scale fluid velocity in porous media.

As important features affecting the transport properties of porous media, dead-end and closed-pore structures have been investigated for several decades [39,40]. Moreover, stagnant zones in porous systems, such as eddies or low-speed regions among the preferential flow paths, have been numerically observed either at low or high Reynolds numbers [41–43]. However, the results have always been linked to the medium's structure. Possible variations of these stagnant zones (shape and location) and local flow patterns have not been thoroughly explored.

This study aims to examine systematically the flow structures at the pore scale over the Darcy regime with a focus on the flow tortuosity. A static porous medium composed of fixed spherical particles (with no-slip boundaries) is employed. We also investigate the flow behavior in dynamic porous media. In this case, we are interested in active porous structures in which the porosity remains constant (e.g., exothermic porous media [44]), eliminating the effects of porosity variation on the permeability. Such an active condition is obtained by using the particles constantly spinning with different angular velocities around fixed axes.

Fluid flow due to rotating spheres is of intrinsic interest in fluid dynamics, meteorology, astrophysics, and many other fields. It has received much attention theoretically, numerically, and experimentally [45–47]. Here, we investigate pore fluid structures in a pack of rotating spheres that also undergo a general flow crossing the medium. The rotation of spheres may appear in certain conditions, for example, under Quincke effects [48]. The rotating sphere pack is generally considered an example of dynamic media. Fluid flow in dynamic porous media can have prospective applications in physics and industry, for example, dynamic contaminant mobilization in soils [49] or groundwater flow through dynamically loaded sites, e.g., via vehicles, piling construction, or machinery foundations.

Apart from that, we examine the validity of Darcy's law where the fluid is subject to internal sources of energy from the medium (as a disturbance energy), and yet the net flow is driven by the macroscopic pressure gradient (or body force). The macroscopic linearity as per Darcy's law is tested in the presence of highly variable microscopic flow behavior. The findings have implications for the "universality" of the concept of constant (structure-dependent) flow tortuosity within the Darcy regime, which is the

implicit assumption lying at the root of the models that describe flow (and transport) in porous media. We are interested in the portion of pore space that contributes to the flow of the passing-through fluid (the Darcy flux). The mechanism underlying the pore-scale flow behavior is also investigated.

II. METHODOLOGY

We conduct numerical simulations using a computer model based on the lattice-Boltzmann method (LBM) and the discrete-element method (DEM) [50]. The simulated porous medium is made of 500 spherical particles, each of 16 lattice units (l.u.) in diameter, randomly deposited into a box with a cross section of 182×182 l.u. In the LBM, the variables are defined in lattice units and time steps but can be converted to physical units based on dimensionless numbers, e.g., Reynolds numbers [51]. The model dimensions and the particle diameter are convertible to physical units of 9 mm for the sphere diameter and 10×10 cm for the cross section of the box domain with water being the fluid. The packing of particles is obtained with the simulation of a natural deposition through a free-fall process using the discrete-element method resulting in a medium with the porosity of $\phi = 0.42$. This medium is then imported into the LBM model where the fluid flow through the pore space is simulated. When the spheres settle into the box, they spin (with different angular velocities) in their location for some time depending on the surface friction specified. To generate static porous media, the angular velocities of the spheres are set to zero after deposition is completed (zero linear velocities). In contrast, the spheres in dynamic porous media are fixed in their locations (with zero linear velocity) but keep rotating at constant angular velocities caused by the deposition process. In the dynamic porous medium, each sphere is spinning at a different but constant angular velocity over time [Fig. 1(a)] around a fixed axis [with a different orientation from others; Fig. 1(b)]. While the angular velocity distribution depicted in Figs. 1(a) and 1(b) is referred to as the ω_0 dynamic case, other dynamic conditions are also simulated by multiplying the angular velocity of each sphere by a constant factor (0.5 and 2) but maintaining the same axes of rotations.

The process of particle deposition by which the initial rotations of the spheres are induced is a natural example that makes the preferential direction of rotations: the particles in contact with others will rotate in directions and speeds correlated by the relative movement of others. The rotation of particles in our model is then not a random but a correlated distribution. By maintaining the rotations in dynamic media, we suggest that a natural condition in which preferential movements of particles are induced (e.g., rearrangement of packings by continuous shear strains) can be mimicked.
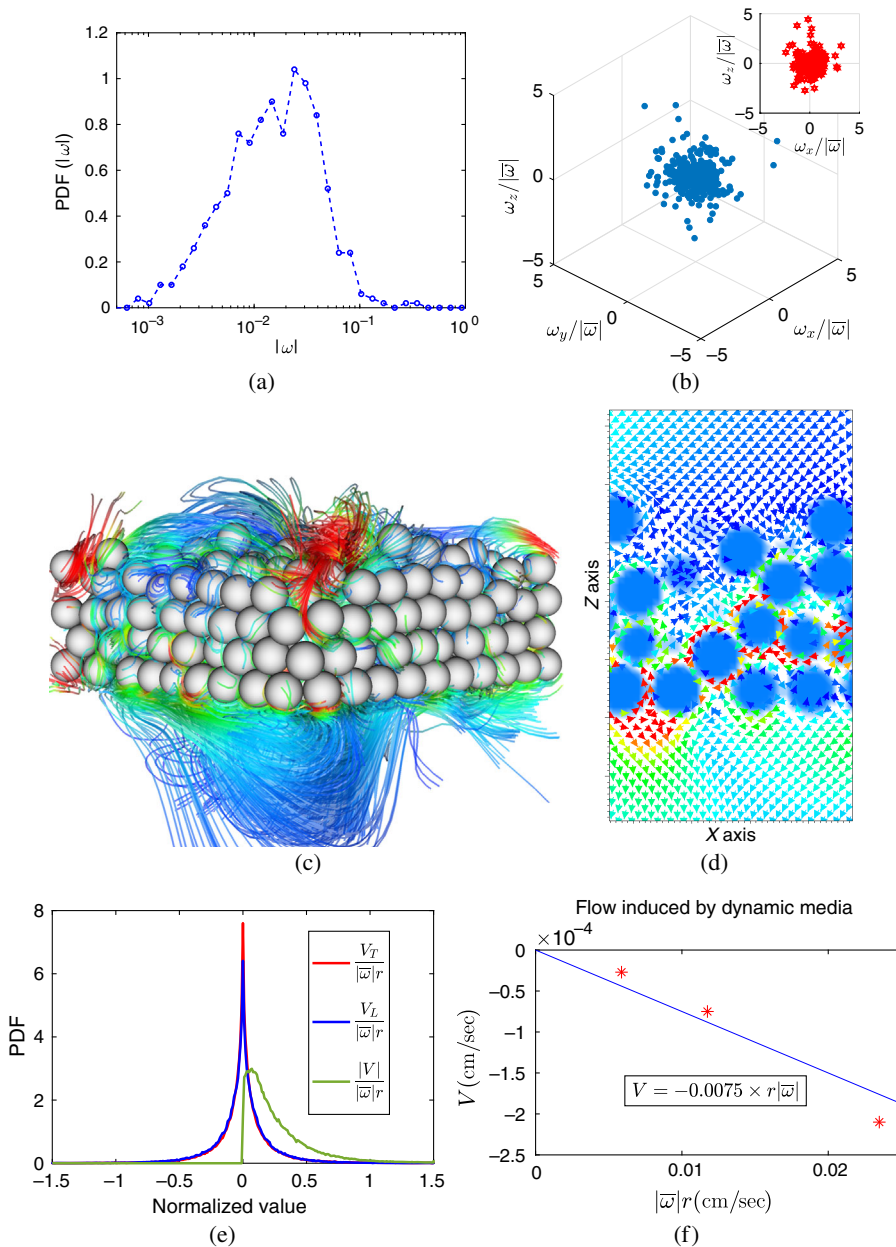
(a)

(b)

(c)

(d)

(e)

(f)

FIG. 1. Dynamic porous media with periodic boundary conditions. (a) Probability density function (PDF) of the magnitudes of angular velocities $[|\omega|(\mathrm{rad/sec})]$ imposed to the spheres to produce dynamic porous media (resulting from the natural deposition process as we describe in Sec. II). Each particle of such media is rotating at a different but constant $\omega = (\omega_x, \omega_y, \omega_z)$ around a fixed axis also different in orientation from the others. The mean of the rotation speed magnitudes is equal to $|\bar{\omega}| = 0.026$ rad/sec. (b) The orientation of rotations displayed as angular velocity components. (c) Streamlines for the dynamic porous medium. Here, the boundary conditions for all sides of the model are periodic (no pressure or velocity boundary conditions); thus, the resulting flow (downward) is caused by the rotating spheres only. (d) The velocity vectors shown on an internal cross section of this model, indicating the main direction of flow ($-z$, negative longitudinal) indicated by the rotating sphere pack. (e) Pore fluid velocity distributions of the rotating sphere pack for longitudinal (V_L) and transverse (V_T) velocities and velocity magnitudes ($|V|$). (f) The macroscopic velocity of outflow caused by the rotating sphere system (the component in the $-z$ direction) versus $|\bar{\omega}|r$ where r is the sphere radius. The equation shows a linear fitting. The models of rotating spheres are subsequently exposed to additional velocity (pressure) boundary conditions to examine a net Darcy flow (in the $+z$ direction) passing through the dynamic porous medium.

A constant velocity and pressure boundary condition [52,53] are set at the bottom and top of the model domain, respectively, to simulate a constant discharge of fluid through the medium with a constant fluid pressure maintained at the top boundary. Periodic boundary conditions (PBCs) are implemented for the lateral boundaries representing an infinite domain in the lateral directions. The simulations are conducted with different discharge rates to cover the whole Darcy regime (with the post-Darcy conditions also simulated). Each simulation is run until the steady state in flow characteristics (e.g., distribution of velocity and fluid pressure) is reached (normally after 3×10^4 simulation time steps).

More simulations are also conducted to analyze the sensitivity of the results to the number of spheres in the
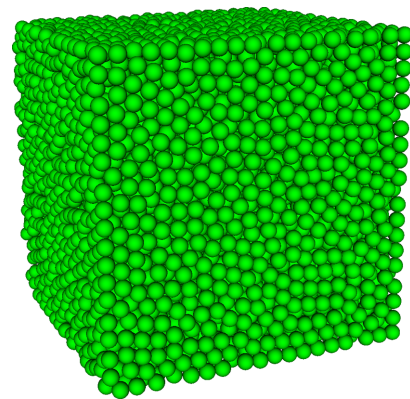

FIG. 2. Monodispersed particle packing achieved by free-fall deposition of 8400 spheres into a box using DEM. The resulting porous medium is then used for LBM simulations.

porous medium (i.e., porous medium dimensions) and the number of lattices per sphere diameter (tested for up to 70 cells/diameter), as well as the lateral boundary conditions (PBC vs no-slip walls). The results reported are found to be unaffected by these factors. For instance, the simulations with 8400 particles with a medium of 200^3 l.u. (PBC for the lateral boundaries, and velocity and density BC for inlet and outlet boundaries, respectively) confirm the consistency of the results (Fig. 2).

III. FLOW REGIME IDENTIFICATION ($V - \nabla P$ RELATIONSHIP)

Based on the simulated (linear) relationship between the pressure gradient across the medium (∇P) and macroscopic flow velocity (V), we determine the Darcy regime (Fig. 3) given by Re $\lesssim$ 1.8, where Re is defined as

$$\mathrm{Re} = \frac{\rho V d_p}{\mu}, \qquad (3)$$

with ρ and d_p being the fluid density and particle diameter, respectively. Within this regime, Darcy's law is indeed found to apply with a constant permeability for the simulated porous media (both static and dynamic).

The straight line fitted to the V versus ∇P relationship for the static porous media passes the origin. However, fitted V versus ∇P lines for dynamic porous media exhibit
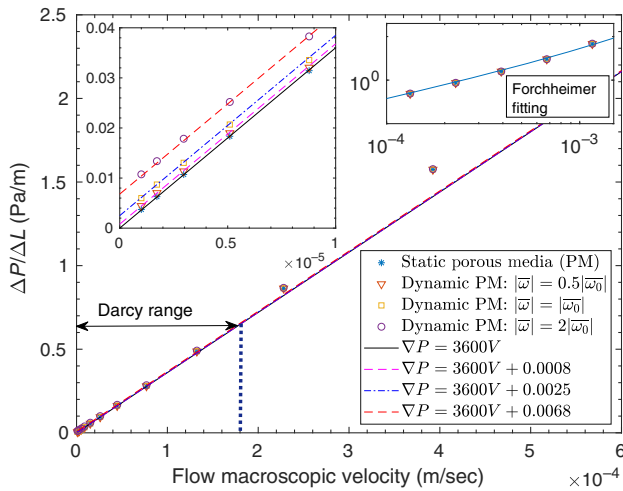

FIG. 3. Pressure gradient versus macroscopic flow velocity for static and dynamic porous media, with the Darcy regime indicated by the linear range, corresponding to Re $\lesssim$ 1.8 (the equations on the figure show the fitting to the Darcy range of the curves). $|\bar{\omega}|$ is the mean angular velocity of the spheres in the dynamic porous media. The permeability of the media within the Darcy regime is found to be the same ($\kappa = 2.78 \times 10^{-7}$ m^2) for all cases. The top left inset shows a close-up near the origin, and the top right inset displays the other end of the graph on a log scale, as the transition to the post-Darcy regime. It also shows the Forchheimer fitting to this part of the curve.

intercepts on the positive part of the ∇P axis. With a higher mean angular velocity for the particles ($|\omega|$), the value of the intercept increases. This behavior can be explained by considering the resulting flow induced by the rotation of spheres. Each spinning sphere can produce a flow around its surface from the two poles (with respect to the axis of rotation) toward the equator and then radially away from it [45]. The resulting pore fluid flow structures appear in the form of vortices. Resulting from the integration of flow generated by the individual spheres, a net flow is induced outward from the medium. The average velocity magnitude of the outflow is presumably proportional to the mean of the tangential velocity of particles $v_\top = |\omega| r$ (with r being the particle radius). The mean of the angular velocities for the dynamic base case is $|\bar{\omega}_0| = 0.026$ rad/sec.

To examine the generation of a net outflow from the system of dynamic spheres, the pack of rotating spheres with the PBC for all boundaries (no velocity boundary conditions) is analyzed (see Fig. 1). In this case, the flow is induced only by the rotating spheres. As an engine made of rotating spheres with different angular velocities around different axes, the system generates a net flow exiting the medium with the longitudinal velocity component in the direction of $-z$ (negative longitudinal). This outflow also results in a gradient of pressure. When we assign the macroscopic flow with velocity boundary conditions in the $+z$ direction (in further simulations for Darcy flow investigation), the net flow overcomes the background flow generated by the rotating sphere system. This combined flow induces a pressure gradient which is the sum of the gradient required to overcome the backward flow and the gradient due to the main flow. With a higher angular velocity of spheres, the net outflow (in the $-z$ direction due to the rotating spheres) is larger. A larger outflow induces a larger background hydraulic gradient across the medium. Thus, for the net macroscopic flow (developed by outer boundary conditions in $+z$), a larger pressure intercept is observed in the V versus ∇P graph (see Fig. 3).

To better understand the mechanism involved in creating a net flow out of the system of rotating spheres, we set up a simple model (Fig. 4). While a rotating sphere produces a symmetrical recirculation zone around it with no net flow in any direction, the symmetry breaking can cause the nonzero net flow in a direction depending on the obstacle location (and the free void space available). A single fixed (nonrotating) sphere next to the same rotating sphere [Fig. 4(b)] accommodates the asymmetric fluid movement that results in an outflow. Two spheres both rotating with the same speed may also produce zero or nonzero net flow depending on the orientations of the rotations. For the same orientation of rotations, the fluid recirculates with no net outflow [Fig. 4(c)]. With opposite orientations of rotation, net flow is produced [Fig. 4(d)]. A similar phenomenon can happen for the medium studied here as the dynamic porous medium which is comprised of spheres rotating individually with

(a) Net flow: $\langle V_z \rangle = 0.0$ (b) Net flow: $\langle V_z \rangle = -0.0104 \, r|\overline{\omega}|$

(c) Net flow: $\langle V_z \rangle = 0.0$ (d) Net flow: $\langle V_z \rangle = -0.0151 \, r|\overline{\omega}|$
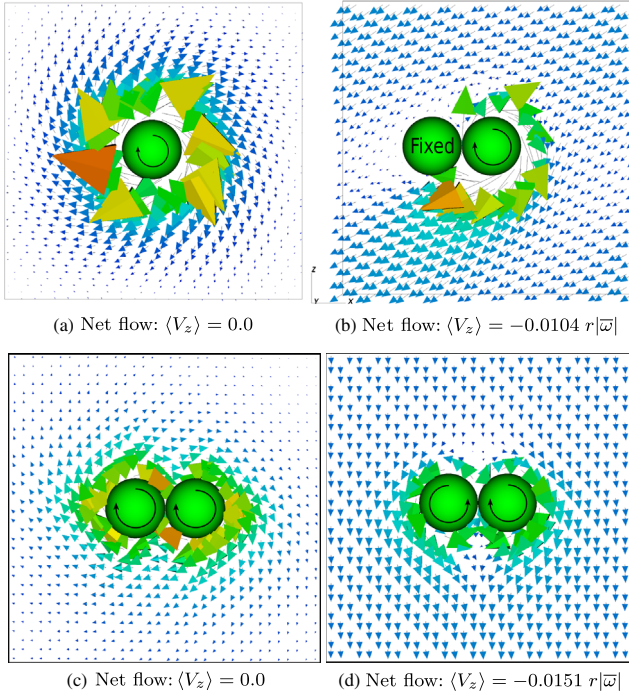
FIG. 4. Simple models to explore the mechanism of the generation of net flow out of the rotating sphere models. The model boundaries are all periodic. (a) A single rotating sphere ($|\omega| = 1.0$ rad/ sec) produces no net flow with the symmetrical recirculation around the rotating sphere. (b) The same rotating sphere when next to a fixed sphere generates a net flow out of the system due to the symmetry breaking for circulating fluid. (c) Two adjacent spheres when rotating with the same orientations produce only local rotational flow but no net flow. (d) Two spheres rotating with opposite orientations generate a net outflow. The combination of differently rotating spheres (different in speed and orientation of rotation) in our porous medium (Fig. 1) can produce complex fluid structures resulting in a net outflow in a similar way as presented here.

various speeds in different orientations. In a packing with the pore space randomly variable, the voids surrounding the particles are not symmetrical, leading to preferential flow directions depending on the relative rotation velocities and the void space available. Spheres may play an obstacle role for neighbors depending on their relative rotations. The complex integration of fluid recirculations and preferential flow streams within the pores provides a net flow out of the medium in a certain direction.

As indicated by Fig. 1(e), the entirely circulating fluid in pore space leads to similar distributions for velocity components in different directions. However, a small net flow is generated in a certain direction out of the medium as discussed earlier. The net flow rate is shown to be more than 2 orders of magnitude smaller than the average of the fluid recirculation velocity, i.e., $|\overline{\omega}|r$ [see Fig. 1(f)].

The intercept on the ∇P axis discussed here is similar to what is well reported as the initial (minimum) pressure gradient (∇P_0) required for the Darcy flow in porous

media [11]; that is, Darcy's law applies only for the pressure gradients greater than ∇P_0, with the new form of $V = -(\kappa/\mu)(\nabla P - \nabla P_0)$. Although the static porous media simulation (no-slip boundary condition for solids) provides no evidence of such an initial pressure gradient, with the dynamic conditions simulated here, the initial pressure gradient is required to generate the net flow through the media. The mechanisms of the initial pressure gradient in nature (the electrical streaming potential, non-Newtonian viscosity, or immobile water layers [54]) and the behavior reported here are different. However, the simulations can be a step toward better understanding of the phenomenon.

The permeability of the porous medium is found to be constant in all conditions (static or dynamic), equal to 2.78×10^{-7} m^2. This value is comparable to the permeability of well-sorted gravels. The medium is made of spheres with a diameter of $d = 9$ mm. Using the Kozeny-Carman equation (2) with $\phi = 0.42$, $S = 6/d$ (as for spheres), $T = 1.168$ (as calculated in our simulations), and $c' = 2.5$ as suggested by Ref. [14], the permeability estimation is equal to 1.45×10^{-7} m^2 which is a close estimation to that of the simulations.

The upper end of the $V - \nabla P$ graph deviates from the linear regime (for Re$\gtrsim 1.8$). As shown in Fig. 3, top right inset, the non-Darcy behavior can be fitted with a Forchheimer equation in the form of [55]

$$\nabla P = \frac{\mu}{\kappa} V + \frac{\rho C_f}{\sqrt{\kappa}} V^2, \qquad (4)$$

with κ being the permeability of the medium obtained from the linear regime, and C_f being the form coefficient taken to be 0.9 here.

IV. STATIC POROUS MEDIA

A. Pore-scale flow variations

Pore fluid velocities obtained from the numerical model are found to vary largely in the longitudinal (L) and transverse (T) directions, as shown in Fig. 5. As expected, the transverse velocity distributions are symmetric about *zero* indicating zero mean velocity in the transverse direction [Fig. 5(b)]. The longitudinal (L) velocities are mostly distributed in the positive range with a small negative tail [Fig. 5(b)]. Further comparisons between our numerical results and experimental and numerical data from the literature are presented in Fig. 5, where a satisfying agreement is observed.

B. Streamlines

Streamlines are computed using the numerical integration [58] on the 3D flow fields obtained from the simulations. As compared in Fig. 6, streamlines in static porous media with different Darcy flow rates show channelized flow mostly directed along the general flow direction.
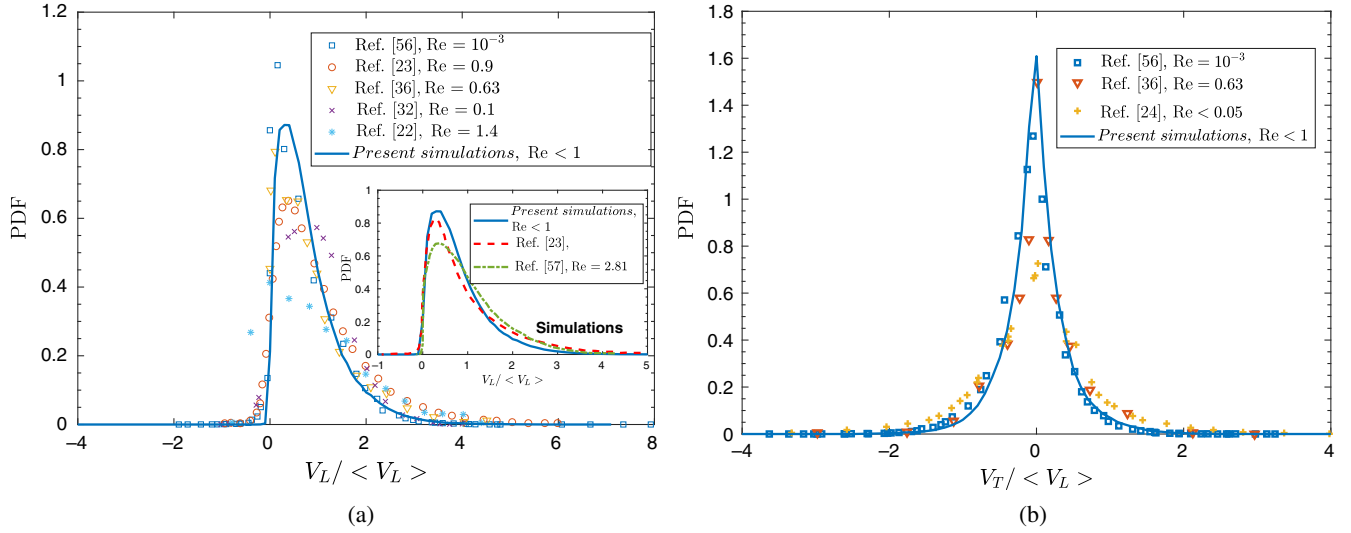
FIG. 5. Static porous media. Probability density functions of the normalized longitudinal V_L (a) and transverse V_T (b) components of velocity obtained from simulations compared to experimental data and also numerical simulation results [(a) inset] from the literature.

Alterations in the shape and direction of streamlines associated with different flow rates within the Darcy regime are negligible.
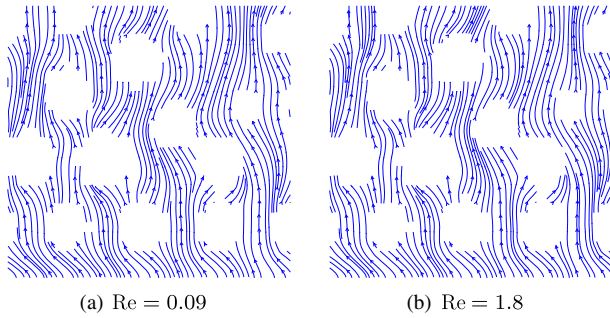

FIG. 6. Static porous media. Flow streamlines for (a) low and (b) high flow rates within the Darcy range.
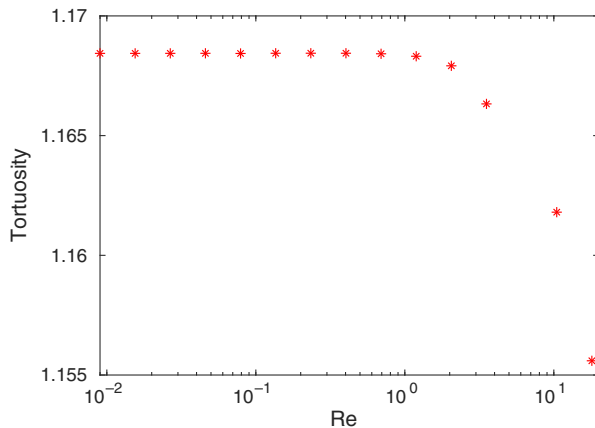

FIG. 7. Static porous media. Variation of the flow tortuosity [Eq. (5)] with flow rate.

C. Tortuosity

The flow tortuosity can be calculated based on the flow velocities [59]

$$T = \frac{\sum v}{\sum v_L},\qquad(5)$$

where v and v_L denote the pore fluid velocity and its component in the direction of macroscopic flow (longitudinal direction), respectively. The method has been used in several studies to investigate the flow tortuosity (e.g., Refs. [19,60,61]). We use Eq. (5) to calculate the tortuosity of the flow in porous media. A cubic section from the middle of the porous media with all sides at a distance from the boundaries is selected as the representative volume for the velocity fields. We use Eq. (5) to calculate the tortuosity of the flow within this cubic section. The results are shown in Fig. 7 where a constant tortuosity $(T = 1.168)$ is observed within the Darcy range. With the flow rate exceeding the upper limit of the Darcy range, tortuosity slightly decreases up to $T = 1.156$ for Re = 18. The decrease in tortuosity can be attributed to the effects of the transition to the non-Darcy regime as also indicated by some researchers (see Ref. [62]).

V. DYNAMIC POROUS MEDIA

In this section, we use the dynamic sphere pack (as we describe in Sec. II) to conduct the flow simulations through the dynamic porous media. The discussion focuses on the case of ω_0 unless mentioned otherwise.
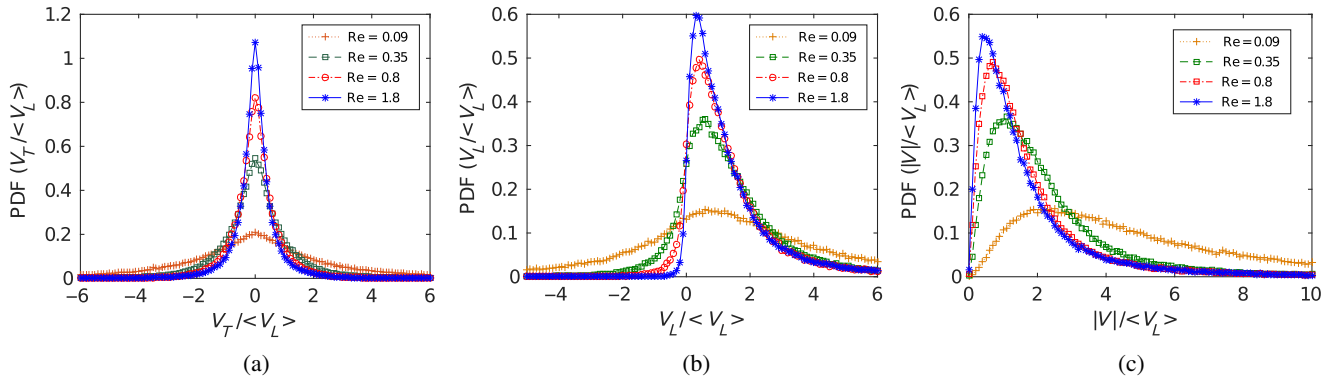
FIG. 8. Dynamic porous media. PDFs of normalized transverse V_T (a) and longitudinal V_L (b) velocity components, and velocity magnitudes (c) obtained from numerical simulations (all within the Darcy range). Under a lower Darcy flow rate, all distributions appear to be wider, with a larger negative portion for V_L; $((V/|\bar{\omega}|r) = 0.95\mathrm{Re})$.

A. Pore-scale flow variations

PDFs of normalized transverse [Fig. 8(a)] and longitudinal [Fig. 8(b)] velocities and velocity magnitudes [Fig. 8(c)] all show wider distributions in the lower Darcy range with smaller macroscopic flow rates (Re). In this range, the countercurrents ($V_L < 0$) are also more profound. The normalized longitudinal flow velocities through the pores display different patterns of flow activities (Fig. 9). Under high macroscopic flow rates, active flow zones appear to be well connected and channelized in the Darcy flow direction [Fig. 9(b)]. In contrast, flow streams under low flow rates are more tortuous with local vortices, separating the pore flow zones into streams directing toward or opposite the main flow direction (countercurrents) [Fig. 9(a)].

With the higher flow rates, the pore flow velocity distributions coincide with those of static medium. This is because the local flow rotational velocities due to dynamic effects are not relatively strong enough to disturb the main flow streams (see Sec. V F for the associated threshold). The transition to unaffected streams is indicated by the decrease of the tortuosity to that of the static conditions (discussed later).

B. Streamlines

The results show different pore-scale flow patterns depending on the macroscopic flow rate or Re (Fig. 10). At low macroscopic flow rates, the fluid moves through very tortuous streamlines, many of which do not even end at the exit boundary and instead form circulation cells inside the medium [Fig. 10(a)]. As the macroscopic flow rate increases, the streamlines become straighter, like those in the static media.

Circulating streamlines under the condition of low macroscopic flow rates in dynamic porous media appear in the form of vortices. The nature of these vortices which are formed in an ideally laminar flow (Darcy regime) [63,64] is different from that of turbulent eddies. Considering that the permeability of the medium is found the same in all of the static and dynamic cases investigated here, we further

examine the mechanism of the flow through dynamic porous media with identification of the conducting flow channels and recirculating fluid capsules (no net flow).

C. Vorticity

We compute the vorticity based on the simulated flow velocity, i.e., the curl of the velocity vector. The variation of
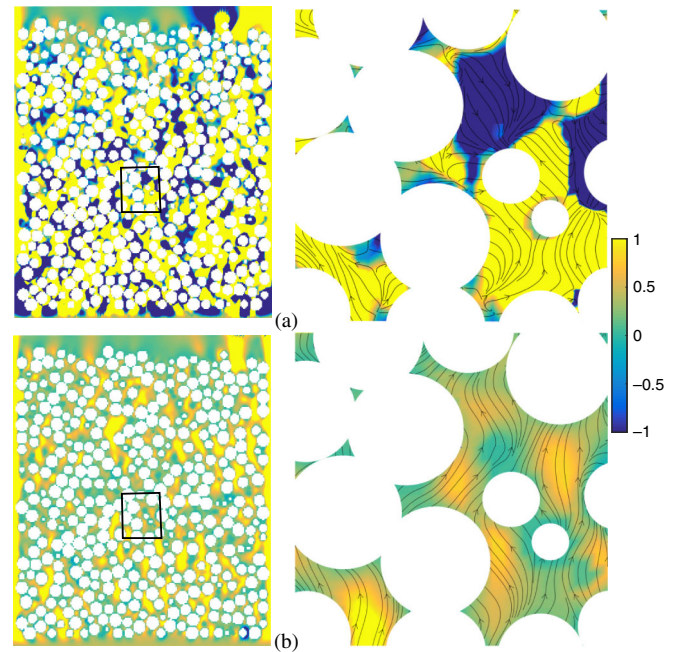

FIG. 9. Dynamic porous media. Normalized longitudinal velocity $((V_L/\langle V_L \rangle))$ in a cross section at the middle of the 3D model, for (a) Re = 0.025 $((V/|\bar{\omega}|r) = 0.024)$ and (b) Re = 2 $((V/|\bar{\omega}|r) = 1.9)$. The color scale is adjusted so that the normalized velocities greater (or smaller) than 1 (or −1) are shown in the same color. Thus, the color map mainly differentiates the positive and negative longitudinal velocities (countercurrents). Small zones at the middle indicated with squares on the left are magnified at right panels, also showing the streamlines. The macroscopic Darcy flow direction is upwards.

(a) Re = 0.09 ($\frac{V}{|\bar{\omega}|r} = 0.085$)
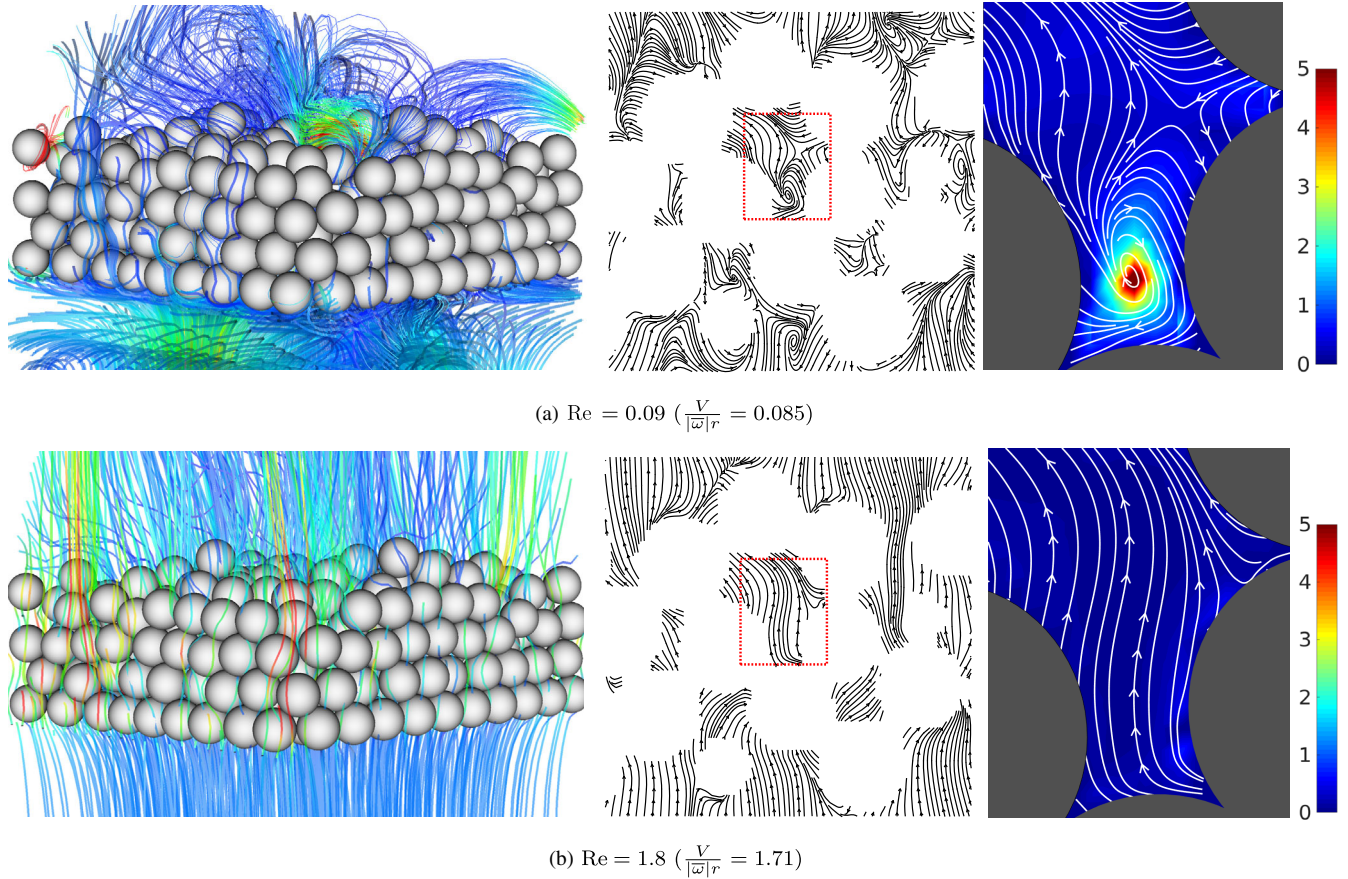

(b) Re = 1.8 ($\frac{V}{|\bar{\omega}|r} = 1.71$)

FIG. 10. Dynamic porous media. Flow streamlines shown in 3D (left) and in 2D (middle) at a vertical section of the modeled porous medium for a low (a) and high (b) flow rate both within the Darcy range. A single-pore zone from the selected section is enlarged at the right-hand side with color images showing the normalized vorticity.

the curl magnitude within the pore space is investigated. For the purpose of comparing the flow structures of different Darcy flow rates, we normalize the curl magnitude by the macroscopic flow velocity. That is, the curl is first calculated over normalized velocity fields and then divided by local normalized velocity magnitude, i.e., $|\nabla \times (v/\langle v\rangle)|/|v/\langle v\rangle|$. As shown in Fig. 10(a), the zones of curl magnitudes with converged gradients can be identified as vortices and linked to circulating streamlines under the condition of low macroscopic flow rates in dynamic porous media. While some vortices appear to circulate solid particles, smaller vortices also exist entirely within the pore space. The vortex flow structures, however, disappear in cases with larger macroscopic flow rates (Re) within the Darcy regime [Fig. 10(b)].

Combining the results of streamline and curl magnitude, we determine a critical value of the normalized curl magnitude (Ω_0) to separate the vortical zone (pore space occupied by vortices) and the passing-through flow zone (pore space with streamlines passing through the whole medium). When the macroscopic flow rate is low (Re → 0), the vortical zone caused by spinning particles dominates, but such a dominance diminishes as the macroscopic flow

rate increases (Re $\gtrsim$ 1), and the whole pore space contributes to the passing-through flow toward the upper end of the Darcy regime (Re ≈ 1.8) [Fig. 13(c)]. The volume of pore space contributing to the passing-through flow [denoted as *net flow streams* in Fig. 13(c)] increases with the Darcy flow rate reaching the maximum value (entire pores) at high flow rates.

The generation of the vortices can be characterized by the value of $(V/|\bar{\omega}|r)$ (see Fig. 11). For values less than 1, the main flow rate is weaker than the rotational streams, resulting in evolving vortices. As this ratio increases, the main flow gradually overwhelms the rotational zones, making the vortices progressively shrink and transform to channelized flow streams for $(V/|\bar{\omega}|r) > 1$.

D. Tortuosity

1. Tortuosity calculated using streamlines

The results that we present above for dynamic porous media demonstrate large variations of pore-scale flow behavior with different characteristics over the same macroscopic Darcy flow regime (with invariant permeability). To quantify such variations, we compute flow tortuosity, a

(a) Re = 0.015 ($\frac{V}{|\bar{\omega}|r} = 0.0145$)   (b) Re = 0.09 ($\frac{V}{|\bar{\omega}|r} = 0.085$)   (c) Re = 0.135 ($\frac{V}{|\bar{\omega}|r} = 0.128$)

(d) Re = 0.69 ($\frac{V}{|\bar{\omega}|r} = 0.66$)   (e) Re = 1.17 ($\frac{V}{|\bar{\omega}|r} = 1.11$)   (f) Re = 10.44 ($\frac{V}{|\bar{\omega}|r} = 9.91$)
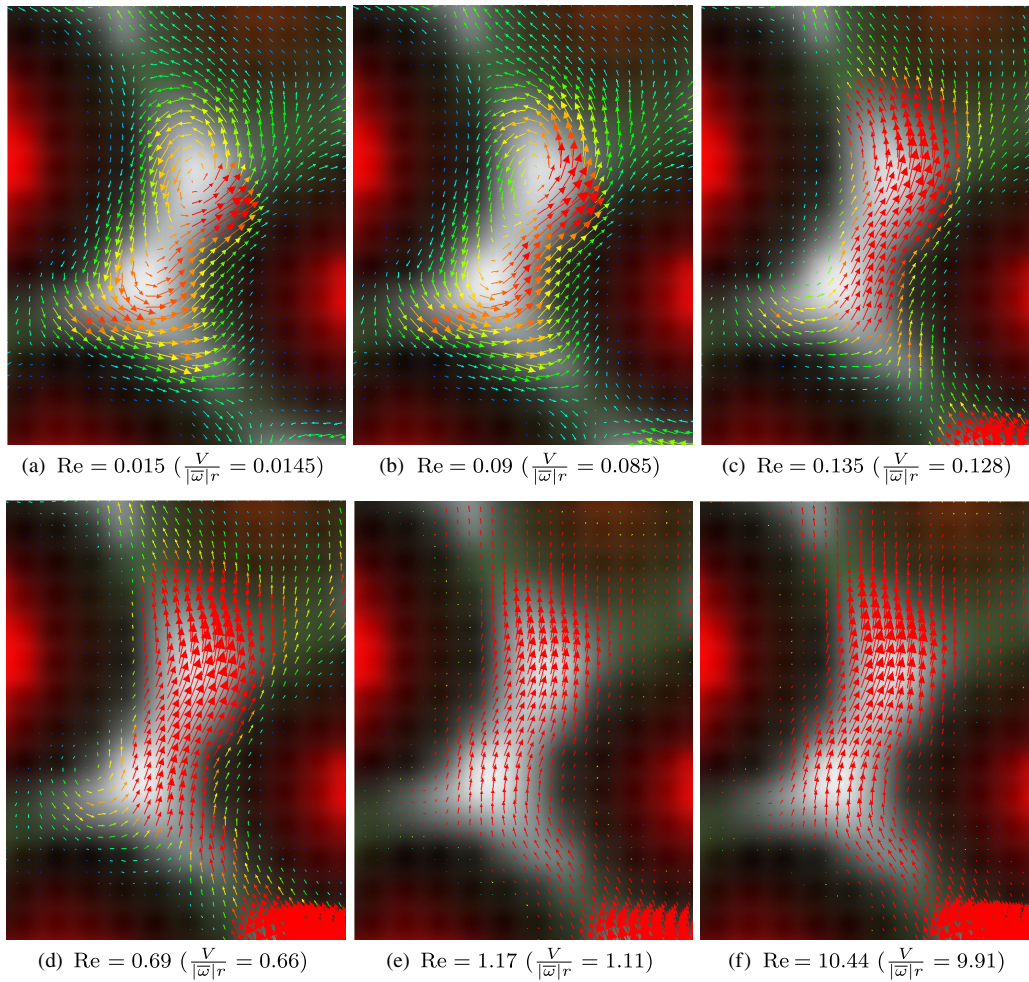
FIG. 11. Dynamic porous media. Vortex progressive dissipation. The vortices are generated by the effects of rotating spheres. As the Darcy flow becomes relatively stronger, indicated by a larger $(V/|\bar{\omega}|r)$, the vortices progressively disappear and the flow becomes channelized.

quantity often treated as a function of only porosity in porous media flow studies [19,60,65–69]. With the streamlines already computed, the tortuosity of the streamlines can be calculated as the ratio of l/L, where l is the actual length of the streamline, and L is its direct length in the macroscopic flow direction. The PDF of the tortuosity values calculated for all individual streamlines (Fig. 12)
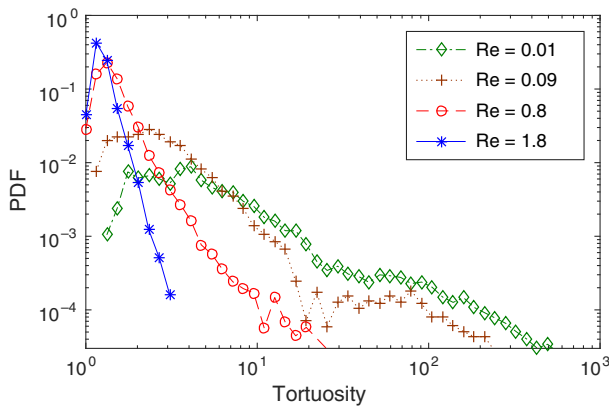

FIG. 12. Dynamic porous media. PDF of the tortuosity values of all streamlines for different flow rates, all within the Darcy range; $(V/|\bar{\omega}|r = 0.95\text{Re})$.

indicate a highly variable behavior of the flow in dynamic porous media: at low flow rates, streamlines have a wide range of tortuosities including a portion of highly tortuous streamlines. At high flow rates, the tortuosity values span a narrow range, mostly less than 2. In all cases, there are a number of streamlines with small tortuosities ($T < 2$), which are the passing-through streamlines, but their proportions to all streamlines vary largely with the Darcy flow rate.

The average of the flow tortuosity is also first calculated directly from all the streamlines, i.e., the ratio of the sum of the streamlines' actual lengths ($\sum l_i$) to the sum of their length in the macroscopic flow direction ($\sum L_i$). Given that some streamlines belong to vortical regions with no share in the net flow, this method provides a tortuosity value associated with all pore fluid movements regardless of contributions to the net flow. A decreasing trend in the calculated tortuosity from large values of the order of 10^2 at low Darcy flow rates to small values less than 2 at the upper limit of the Darcy range is observed [Fig. 13(b), all streamlines]. While the tortuosity variation reflects the changes of pore fluid flow structures over the Darcy regime, the calculated tortuosity cannot be linked directly to the macroscopic passing-through Darcy flow. Therefore,
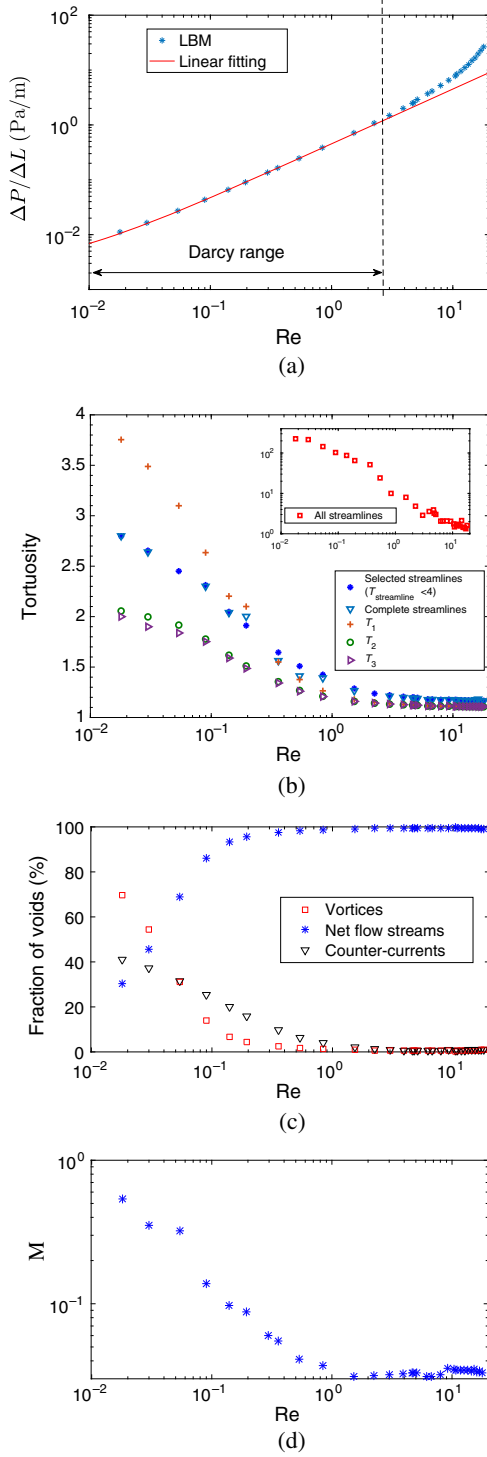
FIG. 13. Dynamic porous media. (a) Averaged fluid pressure gradient across the porous medium versus Re showing the Darcy flow regime studied ($V/|\bar{\omega}|r = 0.95$Re). (b) Variations of calculated tortuosity based on different methods. (c) The fraction of pore space occupied by different flow regions. (d) Variations of the $M = (\sigma P/d_p)/(\Delta P/\Delta L)$. σP, d_p, and ΔP are the standard deviation of the fluid pressure calculated at the lower (entrance) boundary of the porous medium, particle diameter, and the macroscopic fluid pressure difference across the medium with the macroscopic length of ΔL, respectively.

we recalculate the tortuosity based on only passing-through streamlines, those that span the medium from the bottom (net flow entrance) to top (net flow exit) boundary [Fig. 13(b), complete streamlines]. Another criterion is also applied to select additional streamlines that are likely to belong to the passing-through group but do not appear to exit the medium. The criterion is that streamlines whose individual tortuosity is less than 4 with an ending point located at the highest elevation of the streamline path are also passing-through streamlines [Fig. 13(b), selected streamlines]. The threshold of 4 is chosen according to the outcomes of the other methods we explain below (i.e., T_1), which show that the passing-through flow has a maximum tortuosity less than this value. A sensitivity analysis confirms the rationale of this threshold.

2. Tortuosity calculated over velocity fields

While being popular as a preferred method to calculate the tortuosity, Eq. (5) has some limitations [19] that clearly exist when applied to complex flows as encountered here. Thus, modifications are needed to exclude the effects of counter-currents and circulations that make no contribution to the macroscopic flow through the whole porous medium. The following modified tortuosity equations are introduced,

$$T_1 = \frac{\sum v}{\sum v_{L(v_L>0)}}, \qquad (6)$$

$$T_2 = \frac{\sum v_{(v_L>0)}}{\sum v_{L(v_L>0)}}, \qquad (7)$$

$$T_3 = \frac{\sum v_{(\Omega<\Omega_0)\wedge(v_L>0)}}{\sum v_{L(\Omega<\Omega_0)\wedge(v_L>0)}}, \qquad (8)$$

with the parameters defined as follows: $v_{L(v_L>0)}$ are the longitudinal-component velocities for those velocity vectors with positive L components (directing in the macroscopic flow direction, i.e., $+L$), $v_{(v_L>0)}$ are the velocities with positive L components, $v_{(\Omega<\Omega_0)\wedge(v_L>0)}$ and $v_{L(\Omega<\Omega_0)\wedge(v_L>0)}$ are velocities and L-component velocities for those vectors with positive L components and the curl magnitudes less than the critical value of Ω_0. These modified equations [Fig. 13(b)] give similar results to those calculated based on passing-through streamlines. In summary, the calculated tortuosity based on all streamlines for the dynamic porous medium varies by 2 orders of magnitude over the Darcy regime, consistent with the large changes of pore-scale flow structures. With the vortical zone excluded, the tortuosity of the conducting channels given consistently by different methods remains variable but to a much less extent (by a factor of 2).

E. Pressure fluctuation

We also analyze local pore fluid pressure fluctuations (spatial variations) relative to the global pressure drop

across the medium. A dimensionless number is introduced, i.e.,

$$M = \frac{\frac{\text{Mean of local fluid pressure fluctuations}}{\text{Specific length}}}{\text{Global pressure gradient}}. \qquad (9)$$

For the mean of local fluid pressure fluctuations, the standard deviation of fluid pressure σ_P is evaluated at the lower boundary of the porous medium, while the specific length is chosen as the particle diameter. Over the Darcy regime, this dimensionless number is found to vary in a similar manner to that of the tortuosity [Fig. 13(d)]. We suggest that the similarity is linked to the mechanism of the pore-scale flow behavior. Local pressure fluctuations can potentially induce vortical flow (or be caused by such a flow), depending on the intensity of the net (global) flow. Large local pressure fluctuations under a weak net flow condition (small global pressure drop) as indicated by a large M number tend to produce vortical, tortuous pore-scale flow structures.

F. General range of tortuosity variation

With different speeds of rotations for the spheres in the porous medium, the velocity of disturbed (vortical) pore fluid changes. We examine the effects of rotation speeds by changing the angular velocity of spheres ($n\omega_0$). The results show that the increase of rotation speeds causes a larger tortuosity of the flow (Fig. 14), and yet the permeability remains constant (see Fig. 3).
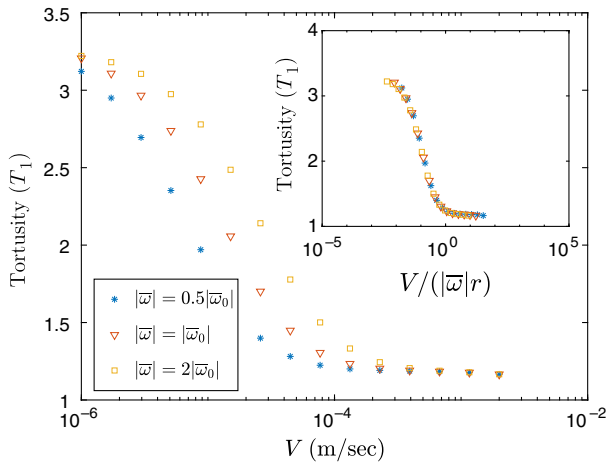

FIG. 14. Dynamic porous media. Tortuosity vs flow macroscopic velocity (V) for porous media of rotating particles with different mean angular velocities ($|\bar{\omega}|$). Here, V is the velocity of net flow passing through the dynamic medium which is controlled by external boundary conditions. The inset shows the tortuosity vs $V/|\bar{\omega}|r$ where r is the particle radius. The unique relationship indicates that when the mean flow velocity (V) reaches the mean velocity of disturbed pore fluid motions due to rotating spheres ($|\bar{\omega}|r$), the effects of the dynamic medium on flow diminish, and the flow retrieves the minimum tortuosity equivalent to that of static media.
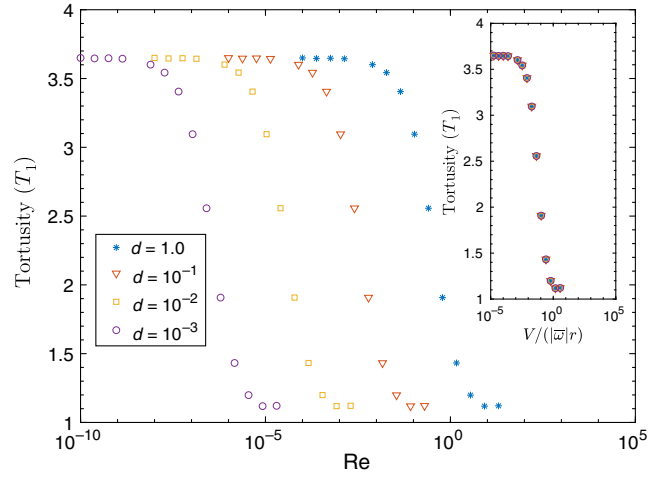

FIG. 15. Dynamic porous media. Tortuosity vs Reynolds number for dynamic porous media of spheres with different sizes. d_p is the spherical particle size (in centimeters). The spheres rotate on average with angular velocity of $4.3|\bar{\omega}_0|$. The inset shows the tortuosity vs $V/|\bar{\omega}|r$ where all curves collapse into a single relationship. Here, V is the flow macroscopic velocity, and $|\bar{\omega}|$ is the mean of the angular velocity of spheres.

A unique relationship is found between the tortuosity of flow and the dimensionless number of $V/|\bar{\omega}|r$ (Fig. 14, inset). With the net flow velocity (V) exceeding the mean tangential velocity of spheres ($|\bar{\omega}|r$), the tortuosity drops to the minimum possible value that coincides with that of the static medium. Thus, $V = |\bar{\omega}|r$ can be taken as the threshold of dynamic porous medium effects on local pore fluid velocity distributions (tortuosity).

G. Effects of the medium's characteristic length

We examine the effect of variations in particle diameter on the flow behavior under the dynamic porous media circumstances. The simulations are performed for the media comprised of particles with diameters of 1.0 to 10^{-4} in the unit of length (with water as the fluid and sizes
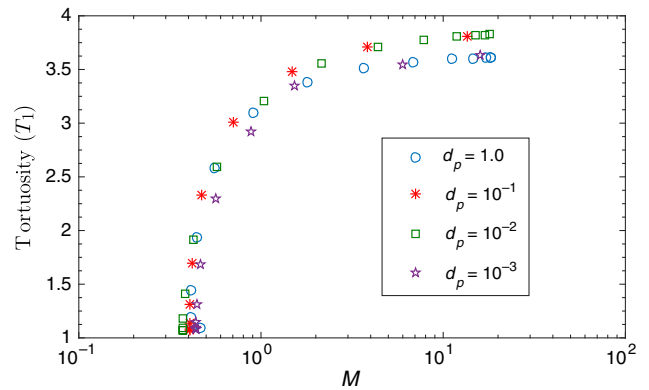

FIG. 16. Dynamic porous media. Tortuosity vs M number (as defined for Fig. 13). d_p is the spherical particle size (in centimeters).

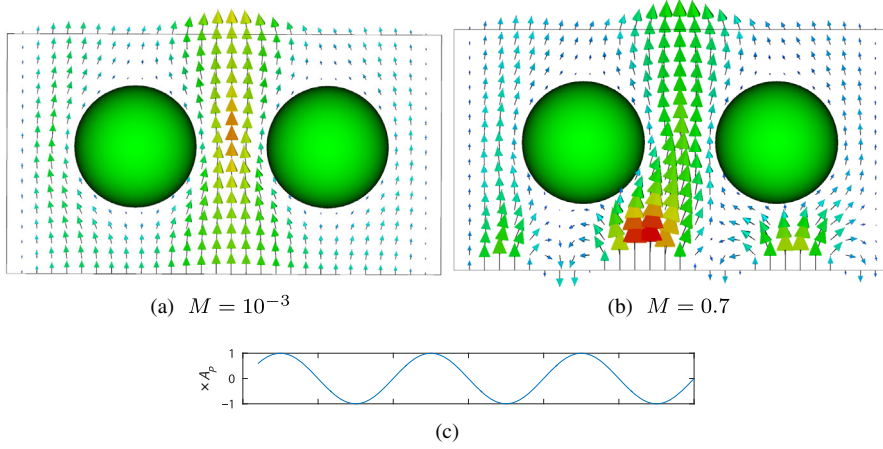(a) $M = 10^{-3}$ (b) $M = 0.7$

(c)

FIG. 17.   Velocity vectors for a simple double-sphere model. In this model, pressure boundary conditions are imposed to the upper (outlet) and lower (inlet) boundaries as constant and sine waves, respectively. The overall ΔP is the same in both cases, while the M number ($M = $ (Amplitude of pressure sine wave/Macroscopic pressure difference) $= A_P/\Delta P$) is different [$M = 10^{-3}$ (a) and 0.7 (b)]. The pressure applied at the lower boundary is equal to $P_0 + \Delta P + P_{\text{wave}}$, where P_0 is the pressure at the upper boundary, and P_{wave} is a function of the lateral coordinate in the form of (c).

in units of centimeters). The angular velocity distribution is determined in the same way as shown in Fig. 1(a) but multiplied by a constant factor of 4.3 for all spheres.

The tortuosity varies with the flow rate and the characteristic length (Fig. 15). As expected, the flow disturbance resulting from the rotation of particles can alter the tortuosity, while the range of this effect varies with the particle diameter. The velocity of disturbed (circulating) fluid is a function of the tangential velocity of particles ($v_\top = |\omega| r$). Hence, with a decrease in particle diameter, the range of Reynolds numbers in which the tortuosity varies is reduced to the same orders as that of r^2.

A unique relationship is found between the tortuosity and the M number (Fig. 16). This indicates a similar relative local pressure fluctuation with respect to the flow tortuosity, regardless of the porous medium characteristic lengths. The uniqueness of the T versus M relationship provides a measure to integrate the flow characteristics in pore scale. With the interrelationship between flow tortuosity and the local pressure fluctuations, the circumstances where one may cause the other can be further identified.
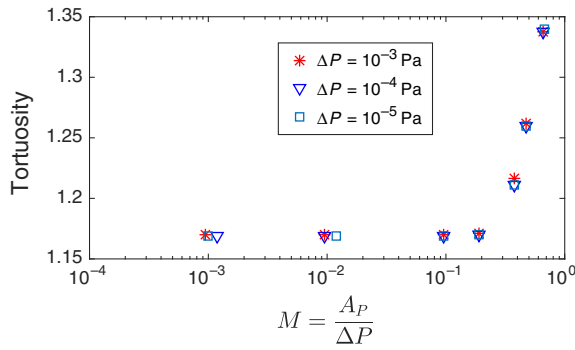

FIG. 18.   Variations of the M number ($M = A_P/\Delta P$) and flow tortuosity (T_1) under conditions of different macroscopic pressure gradients obtained from the simple double-sphere model (Fig. 17).

VI. PRESSURE FLUCTUATION-TORTUOSITY RELATIONSHIP

To further explore the mechanism behind the tortuosity variations, we set up a simple model with only two spheres representing the solid phase and confining the pore space where the fluid flows (see Fig. 17). This simple medium is subjected to different pressures at the lower and upper boundaries. While the upper boundary pressure is set to be spatially uniform (P_0), the lower boundary pressure oscillates spatially in a sinusoidal form ($P = P_0 + \Delta P + A_p \times \sin(\pi/5 \times i)$), where A_P is the pressure fluctuation amplitude, and i is the lateral coordinate in lattice units for the spheres with diameter of 8 l.u. The simulations are conducted under various conditions with different averaged pressure drop over the medium and different amplitudes and wavelengths of the sinusoidal pressure oscillations at the lower boundary. For this model, the M number is given by $M = A_P/\Delta P$, where ΔP is the average pressure difference between the boundaries. The results clearly demonstrate that local fluid pressure fluctuations in counterbalance with the global (averaged) pressure gradient cause variations of pore-scale flow behavior over the Darcy regime (Fig. 18). In particular, large pressure fluctuations combined with low global pressure gradients lead to vortical flows in the porous medium. The results also show a strong relationship between M and flow tortuosity, which appears not to be directly affected by the value of the global pressure drop.

VII. CONCLUSIONS

This study provides insights into the pore-scale flow behavior and reveals the vastly different pore-scale flow structures within the Darcy regime in porous media that are subjected to internal energy (here, via spinning particles). The static (ordinary) porous media result in invariant channelized pore-scale flow structures (constant tortuosity). In dynamic porous media, for the lower Darcy ranges (where ($V/|\bar{\omega}| r) < 1$), tortuous flow is shown to produce

vortices with little contribution to the net flux. As the Darcy flow rate increases, vortices shrink in volumes and the channelized flow zones expand. Despite the variations, particularly in flow tortuosity, the macroscopic flow through the medium in the simulated cases satisfies Darcy's law with an invariant permeability for all cases (static and dynamic). The microscopic flow behavior is shown to be linked to the local fluctuations of the pressure compared to the global pressure gradient.

With the variable tortuosity demonstrated here, the findings challenge the universality of the existing porous media models (e.g., the KC model) that relate the medium's permeability to a constant tortuosity. The argument can be more significant in cases where there are considerable internal sources of energy from solid material interacting with the fluid (e.g., geothermal, chemical, or mechanical energies). However, how the flow tortuosity variations that we reveal here are related to an invariant permeability remains a question.

Given that a large portion of pore space occupied by vortices is virtually immobile under relatively low Darcy fluxes for a dynamic medium, how is the solute transport in such a medium? The complex transport mechanism called non-Fickian transport [70,71] has been shown to be an inherent characteristic of many types of porous media (packed and granular media, fractured and open networks), whether homogeneous or heterogeneous [72]. To some extent, can it be related to the pore fluid structures that differ from the ordinary channelized flow? The immobile vortical zones may provide transient storage for solute via exchange with the main solute transport path along the passing-through flow. When examined in realistic porous media conditions, this argument may help us to better understand complex transport mechanisms in porous media. The solute transport mechanisms with respect to the variable pore flow behaviors, thus, require further investigations.

ACKNOWLEDGMENTS

---

[1] Derek Ingham, Adrian Bejan, Eden Mamut, and Ian Pop, *Emerging Technologies and Techniques in Porous Media* (Springer Science & Business Media, New York, 2012), Vol. 134.

[2] Kambiz Vafai, *Porous Media: Applications in Biological Systems and Biotechnology* (CRC Press, Baco Raton, 2010).

[3] Stéphane Bonelli, *Erosion of Geomaterials* (John Wiley & Sons, New York, 2012).

[4] Clifford K. Ho and Stephen W. Webb, *Gas Transport in Porous Media* (Springer, New York, 2006), Vol. 20.

[5] Chongbin Zhao, *Physical and Chemical Dissolution Front Instability in Porous Media* (Springer, New York, 2014).

[6] A.-R. A. Khaled and K. Vafai, The role of porous media in modeling flow and heat transfer in biological tissues, Int. J. Heat Mass Transfer **46**, 4989 (2003).

[7] J. Ranft, J. Prost, F. Jülicher, and J.-F. Joanny, Tissue dynamics with permeation, Eur. Phys. J. E **35**, 46 (2012).

[8] Matthew M. Mench, *Fuel Cell Engines* (Wiley Online Library, New York, 2008).

[9] Arun S. Mujumdar, *Handbook of Industrial Drying* (CRC Press, Baca Raton, 2014).

[10] João M. P. Q. Delgado, *Industrial and Technological Applications of Transport in Porous Materials* (Springer, New York, 2013).

[11] Jacob Bear, *Dynamics of Fluids in Porous Media* (American Elsevier Publishing Company, New York, 1972).

[12] Josef Kozeny, Uber kapillare leitung der wasser in boden, R. Acad. Sci., Vienna, Proc. Class I **136**, 271 (1927).

[13] Phillip C. Carman, Fluid flow through granular beds, Chem. Eng. Res. Des. **75**, S32 (1997).

[14] Phillip C. Carman, Permeability of saturated sands, soils and clays, J. Agric. Sci. **29**, 262 (1939).

[15] Philip Crosbie Carman, *Flow of Gases through Porous Media* (Academic Press, New York, 1956).

[16] M. Barrande, R. Bouchet, and R. Denoyel, Tortuosity of porous particles, Anal. Chem. **79**, 9115 (2007).

[17] J. Prieur Du Plessis and Jacob H. Masliyah, Flow through isotropic granular porous media, Transp. Porous Media **6**, 207 (1991).

[18] P. Y. Lanfrey, Z. V. Kuzeljevic, and M. P. Dudukovic, Tortuosity model for fixed beds randomly packed with identical particles, Chem. Eng. Sci. **65**, 1891 (2010).

[19] Artur Duda, Zbigniew Koza, and Maciej Matyka, Hydraulic tortuosity in arbitrary porous media flow, Phys. Rev. E **84**, 036319 (2011).

[20] Lihua Shen and Zhangxin Chen, Critical review of the impact of tortuosity on diffusion, Chem. Eng. Sci. **62**, 3748 (2007).

[21] Behzad Ghanbarian, Allen G. Hunt, Robert P. Ewing, and Muhammad Sahimi, Tortuosity in porous media: A critical review, Soil Sci. Soc. Am. J. **77**, 1461 (2013).

[22] Y. E. Kutsovsky, L. E. Scriven, H. T. Davis, and B. E. Hammer, NMR imaging of velocity profiles and velocity distributions in bead packs, Phys. Fluids **8**, 863 (1996).

[23] L. Lebon, L. Oger, J. Leblond, J. P. Hulin, N. S. Martys, and L. M. Schwartz, Pulsed gradient NMR measurements and numerical simulation of flow velocity distribution in sphere packings, Phys. Fluids **8**, 293 (1996).

[24] Antonio Cenedese and Paolo Viotti, Lagrangian analysis of nonreactive pollutant dispersion in porous media by means of the particle image velocimetry technique, Water Resour. Res. **32**, 2329 (1996).

[25] A. J. Sederman, M. L. Johns, A. S. Bramley, P. Alexander, and L. F. Gladden, Magnetic resonance imaging of liquid flow and pore structure within packed beds, Chem. Eng. Sci. **52**, 2239 (1997).

[26] B. Manz, L. F. Gladden, and P. B. Warren, Flow and dispersion in porous media: Lattice-Boltzmann and NMR studies, AIChE J. **45**, 1845 (1999).

[27] Lynn F. Gladden, Magnetic resonance: Ongoing and future role in chemical engineering research, AIChE J. **49**, 2 (2003).

[28] Christopher J. Elkins and Marcus T. Alley, Magnetic resonance velocimetry: Applications of magnetic resonance imaging in the measurement of fluid motion, Exp. Fluids **43**, 823 (2007).

[29] Daniel Bonn, Stephane Rodts, Maarten Groenink, Salima Rafai, Noushine Shahidzadeh-Bonn, and Philippe Coussot, Some applications of magnetic resonance imaging in fluid mechanics: Complex flows and complex fluids, Annu. Rev. Fluid Mech. **40**, 209 (2008).

[30] M. H. Sankey, D. J. Holland, A. J. Sederman, and L. F. Gladden, Magnetic resonance velocity imaging of liquid and gas two-phase flow in packed beds, J. Magn. Reson. **196**, 142 (2009).

[31] Xiaofan Yang, Timothy D. Scheibe, Marshall C. Richmond, William A. Perkins, Sarah J. Vogt, Sarah L. Codd, Joseph D. Seymour, and Matthew I. McKinley, Direct numerical simulation of pore-scale flow in a bead pack: Comparison with magnetic resonance imaging observations, Adv. Water Resour. **54**, 228 (2013).

[32] Monica Moroni and John H. Cushman, Three-dimensional particle tracking velocimetry studies of the transition from pore dispersion to Fickian dispersion for homogeneous porous media, Water Resour. Res. **37**, 873 (2001).

[33] Tetsuya Suekane, Yasuo Yokouchi, and Shuichiro Hirai, Inertial flow structures in a simple-packed bed of spheres, AIChE J. **49**, 10 (2003).

[34] R. Fernández Serrano, M. Iskander, and K. Tabe, 3D contaminant flow imaging in transparent granular porous media, Geotech. Lett. **1**, 71 (2011).

[35] Vishal A. Patil and James A. Liburdy, Turbulent flow characteristics in a randomly packed porous bed based on particle image velocimetry measurements, Phys. Fluids **25**, 043304 (2013).

[36] Rémi Beguin, Pierre Philippe, and Yves-Henri Faure, Pore-scale flow measurements at the interface between a sandy layer and a model porous medium: Application to statistical modeling of contact erosion, J. Hydraul. Eng. **139**, 1 (2013).

[37] Gianluca Blois, Julio M. Barros, and Kenneth T. Christensen, A microscopic particle image velocimetry method for studying the dynamics of immiscible liquid–liquid interactions in a porous micromodel, Microfluid. Nanofluid. **18**, 1391 (2015).

[38] B. D. Wood, S. V. Apte, J. A. Liburdy, R. M. Ziazi, X. He, J. R. Finn, and V. A. Patil, A comparison of measured and modeled velocity fields for a laminar flow in a porous medium, Adv. Water Resour. **85**, 45 (2015).

[39] K. H. Coats and B. D. Smith, Dead-end pore volume and dispersion in porous media, Soc. Pet. Eng. J. **4**, 73 (1964).

[40] A. Koponen, M. Kataja, and J. Timonen, Permeability and effective porosity of porous media, Phys. Rev. E **56**, 3319 (1997).

[41] Eleonora Crevacore, Tiziana Tosco, Rajandrea Sethi, Gianluca Boccardo, and Daniele L. Marchisio, Recirculation zones induce non-Fickian transport in three-dimensional periodic porous media, Phys. Rev. E **94**, 053118 (2016).

[42] K. Chaudhary, M. B. Cardenas, W. Deng, and P. C. Bennett, The role of eddies inside pores in the transition from Darcy to Forchheimer flows, Geophys. Res. Lett. **38**, L24405 (2011).

[43] Branko Bijeljic, Peyman Mostaghimi, and Martin J. Blunt, Signature of Non-Fickian Solute Transport in Complex Heterogeneous Porous Media, Phys. Rev. Lett. **107**, 204502 (2011).

[44] G. Mohan, M. Prakash Maiya, and S. Srinivasa Murthy, Performance simulation of metal hydride hydrogen storage device with embedded filters and heat exchanger tubes, Int. J. Hydrogen Energy **32**, 4978 (2007).

[45] Y. Kohama and R. Kobayashi, Boundary-layer transition and the behavior of spiral vortices on rotating spheres, J. Fluid Mech. **137**, 153 (1983).

[46] S. C. R. Dennis, S. N. Singh, and D. B. Ingham, The steady flow due to a rotating sphere at low and moderate Reynolds numbers, J. Fluid Mech. **101**, 257 (1980).

[47] S. C. R. Dennis, D. B. Ingham, and S. N. Singh, The steady flow of a viscous fluid due to a rotating sphere, Q. J. Mech. Appl. Math. **34**, 361 (1981).

[48] T. B. Jones, Quincke rotation of spheres, IEEE Trans. Ind. Appl. **IA-20**, 845 (1984).

[49] Lakshmi N. Reddi and Sreedhar Challa, Vibratory mobilization of immiscible liquid ganglia in sands, J. Environ. Eng. **120**, 1170 (1994).

[50] S. A. Galindo-Torres, A coupled discrete element lattice Boltzmann method for the simulation of fluid–solid interaction with particles of general shapes, Comput. Methods Appl. Mech. Eng. **265**, 107 (2013).

[51] Michael C. Sukop and Daniel T. Thorne, *Lattice Boltzmann Modeling: An Introduction for Geoscientists and Engineers*, 1st ed. (Springer Publishing Company, Incorporated, New York, 2010).

[52] Shiyi Chen, Daniel Martinez, and Renwei Mei, On boundary conditions in lattice Boltzmann methods, Phys. Fluids **8**, 2527 (1996).

[53] Qisu Zou and Xiaoyi He, On pressure and velocity boundary conditions for the lattice Boltzmann BGK model, Phys. Fluids **9**, 1591 (1997).

[54] M. Kutíĺek, Non-Darcian flow of water in soils-laminar region: A review, Dev. Soil Sci. **2**, 327 (1972).

[55] Haiying Huang, Joseph A. Ayoub *et al.*, Applicability of the Forchheimer equation for non-Darcy flow in porous media, Soc. Pet. Eng. J. **13**, 112 (2008).

[56] Sujit S. Datta, H. Chiang, T. S. Ramakrishnan, and David A. Weitz, Spatial Fluctuations of Fluid Velocities in Flow Through a Three-Dimensional Porous Medium, Phys. Rev. Lett. **111**, 064501 (2013).

[57] Robert S. Maier, D. M. Kroll, Y. E. Kutsovsky, H. T. Davis, and Robert S. Bernard, Simulation of flow through bead packs using the lattice Boltzmann method, Phys. Fluids **10**, 60 (1998).

[58] Tony McLoughlin, Robert S. Laramee, Ronald Peikert, Frits H. Post, and Min Chen, Over two decades of integration-based, geometric flow visualization, Computer Graphics Forum **29**, 1807 (2010).

[59] A. Koponen, M. Kataja, and J. v. Timonen, Tortuous flow in porous media, Phys. Rev. E **54**, 406 (1996).

[60] Hidetaka Saomoto and Jun Katagiri, Particle shape effects on hydraulic and electric tortuosities: A novel empirical tortuosity model based on van Genuchten-type function, Transp. Porous Media 107, 781 (2015).

[61] Y. Jin, J. B. Dong, X. Li, and Y. Wu, Kinematical measurement of hydraulic tortuosity of fluid flow in porous media, Int. J. Mod. Phys. C 26, 1550017 (2015).

[62] R. Sivanesapillai, H. Steeb, and A. Hartmaier, Transition of effective hydraulic properties from low to high Reynolds number flow in porous media, Geophys. Res. Lett. 41, 4920 (2014).

[63] Anoosheh Niavarani and Nikolai V. Priezjev, The effective slip length and vortex formation in laminar flow over a rough surface, Phys. Fluids 21, 052105 (2009).

[64] G. Leneweit and D. Auerbach, Detachment phenomena in low Reynolds number flows through sinusoidally constricted tubes, J. Fluid Mech. 387, 129 (1999).

[65] Maciej Matyka, Arzhang Khalili, and Zbigniew Koza, Tortuosity-porosity relation in porous media flow, Phys. Rev. E 78, 026306 (2008).

[66] Tang Xiao-Wu, Sun Zu-Feng, and Cheng Guan-Chu, Simulation of the relationship between porosity and tortuosity in porous media with cubic particles, Chin. Phys. B 21, 100201 (2012).

[67] Zufeng Sun, Xiaowu Tang, and Guanchu Cheng, Numerical simulation for tortuosity of porous media, Microporous Mesoporous Mater. 173, 37 (2013).

[68] Iuri Freytag and Waldir L. Roque, Influence of granular packing on porosity and tortuosity, Phys. Rev. E 88, 023011 (2013).

[69] Peijun Guo, Lower and upper bounds for hydraulic tortuosity of porous materials, Transp. Porous Media 109, 659 (2015).

[70] S. M. Hassanizadeh, On the transient non-Fickian dispersion theory, Transp. Porous Media 23, 107 (1996).

[71] Shlomo P. Neuman and Daniel M. Tartakovsky, Perspective on theories of non-Fickian transport in heterogeneous media, Adv. Water Resour. 32, 670 (2009).

[72] D. R. Lester, Guy Metcalfe, and M. G. Trefry, Is Chaotic Advection Inherent to Porous Media Flow?, Phys. Rev. Lett. 111, 174101 (2013).